Journal of
Materials Chemistry C

ROYAL SOCIETY
OF CHEMISTRY

PAPER

View Article Online
View Journal | View Issue

Cite this: *J. Mater. Chem. C*, 2023, **11**, 5701

Chiral diketopyrrolopyrrole dyes showing light emission in solid and aggregate states†

Maurizio Mastropasqua Talamo, *[a] Thomas Cauchy, [a] Flavia Pop, *[a] Francesco Zinna, [b] Lorenzo Di Bari [b] and Narcis Avarvari *[a]

Received 25th January 2023,
Accepted 28th March 2023

DOI: 10.1039/d3tc00308f

rsc.li/materials-c

Due to their excellent emissive properties in solution, diketopyrrolo[3,4-*c*]pyrrole (DPP) derivatives are expected to show interesting features in emission in the solid state by suppressing aggregation-caused quenching. In this work, aggregation-enhanced emission (AEE) and circularly polarised light (CPL) emission in the aggregated state have been studied on achiral and chiral DPPs appended with tetraarylethylene units. Both thiophene and phenyl DPPs (**2** and **5**) show classical aggregation-caused quenching (ACQ) of the emission behaviour in the solid state, whereas the presence of triphenylethylene units (**3** and **6**) does not completely quench the emission in the solution state. Nevertheless, enhancement of the emission from the solution to solid state films from 25 to 36% is observed with phenyl DPP (**3**), whereas the less distorted thiophene analogue **6** still shows a classical ACQ behaviour. When the photoluminescence behaviour in the aggregated states was studied in a series of THF/water mixtures, phenyl DPP **3** showed a 2-fold enhancement in fluorescence intensity when the water fraction was increased from 0% up to 70%, accompanied by an increase in the quantum yield from 17% up to 28%, and the achiral compound **8** showed a 3.5-fold enhancement in the fluorescence intensity when the water fraction was increased from 0% to 50%, accompanied by an increase in the quantum yield from 20% up to 58%. Alkylation of DPPs by the Mitsunobu reaction with *N*-*sec*-phenethyl groups has the advantage of enhancing the chiroptical properties in solution due to the proximity of the stereogenic motif. Thus, compound **3**, dissolved at a concentration of 10^{-6} M in $CHCl_3$, emitted detectable CPL under excitation at 365 nm, with $|g_{lum}|$ around 2×10^{-4}, with positive values for the *SS* enantiomer and negative values for the *RR* enantiomer. In this work, we show the importance of the position of the stereogenic motif within the chiral unit and the steric demand of the tetraarylethylene motifs needed to induce light emission in the solid state and CPL emission of chiroptical materials based on DPPs.

1. Introduction

Molecular and polymeric π-conjugated organic materials are key components in the development of organic electronic devices such as systems for energy harvesting, organic light emitting diodes (OLEDs) and transistors (OFETs).[1–5] The advantages of using organic compounds in these optoelectronic technologies include relatively low cost of fabrication, easy processing, and the tunability of the optoelectronic properties (optical absorption, radiative and/or non-radiative relaxation, exciton diffusion, and charge transport) by tailoring the molecular structures and directing the supramolecular organization, *via* expedient chemical synthesis.[6–10] The introduction of molecular chirality into organic optoelectronic materials is currently receiving considerable attention as it can help drive preferential packing modes in the solid state, and also because the interplay between chirality and optoelectronic features can generate chiroptical, magnetochiral and spin-selective properties, which pave the way to a number of feasible innovative technologies ranging from cryptography, quantum photonics, three-dimensional imaging, chiral probes, stereoscopic and/or anti-glare displays with enhanced external efficiency.[1,11–15]

Enantiopure chiral chromophores undergo differential interaction with the two modes of circular polarization of light, namely the left and right Circularly Polarized (CP) light. The differential absorption of these two components results in electronic circular dichroism (ECD), and its measurement constitutes one of the main analytical techniques for the

---

[a] *Univ Angers, CNRS, MOLTECH-Anjou, SFR MATRIX, F-49000 Angers, France. E-mail: maurizio.mastropasquatalamo@univ-angers.fr, flavia.pop@univ-angers.fr, narcis.avarvari@univ-angers.fr*

[b] *Dipartimento di Chimica e Chimica Industriale, Università di Pisa, via G. Moruzzi 13, 56124, Pisa, Italy*

† Electronic supplementary information (ESI) available. CCDC 2237602 and 2237603. For ESI and crystallographic data in CIF or other electronic format see DOI: **https://doi.org/10.1039/d3tc00308f**

characterization of chiral compounds. ECD spectroscopy can indeed deliver precious information about the configurational and conformational composition of a sample and its supramolecular organization.[16–18] In the case of radiative relaxation in an excited state, left and right polarizations are emitted differently, which amounts to circularly polarized luminescence or CPL. CPL can be quantified by the dissymmetry factor defined as $g_{\text{lum}} = 2(I_L - I_R)/(I_L + I_R)$, where I_L and I_R are the intensities of the left- and right-handed circularly polarised emitted lights, respectively.[19,20] Moreover, another expedient metrics is CPL brightness (B_{CPL}), which beside g_{lum} takes into account the extinction coefficient (ε) and the quantum yield (φ), as $B_{\text{CPL}} = \varepsilon \cdot \varphi \cdot |g_{\text{lum}}|/2$.[21]

Chiral lanthanide complexes have been long studied as CP light emitters, displaying large $|g_{\text{lum}}|$ values, sometimes exceeding unity.[22,23] However, light emission from lanthanide complexes may suffer from modest quantum yields and is severely limited by the absence of any tunability. In order to facilitate the development of CPL-based applications, chiral systems containing organic fluorophores displaying high fluorescence quantum yields and tuneable photophysical properties are currently gaining increasing interest as CP light emitters. Most of the explored CPL emitting organic molecular systems rely on achiral chromophores, chirally perturbed by the introduction of stereogenic motifs such as elements of point, axial, helical or planar chirality.[24–28]

1,4-Diketo-3,6-diarylpyrrolo[3,4-*c*]pyrrole (DPP) derivatives are a class of dyes based on a rigid bilactam core conjugated with two aromatic side groups, known for their intense optical absorption and high fluorescence quantum yields. By varying the nature of the flanking aryl groups, it is possible to tune the HOMO–LUMO gap from the green to the near-infrared (NIR) domain.[24,29,30] On the other hand, the substituents on the nitrogen position only slightly affect the optical features of isolated DPP dyes but have a huge impact on the intermolecular interactions, the packing modes and hence the photophysical properties in the solid state.[6,31] Due to their rigid structures and the extended π-conjugation, the DPP derivatives display aggregation modes often dominated by π-stacking interactions, which eventually lead to the phenomenon known as Aggregation-Caused Quenching (ACQ) consisting of a dramatic reduction of the fluorescence yield upon aggregation. However, sterically demanding groups can reduce the extent of π-stacking interactions, preserving decent emissive properties in the solid state.[6,32]

Owing to their advantageous photophysical properties, DPP dyes have been studied in few cases as molecular systems for CP light emission: DPP dyes chirally perturbed by enantiopure binaphthyl side groups reached $|g_{\text{lum}}|$ values of 6×10^{-4},[25] while chiral dyads of DPP units bridged through an enantiopure helicene displayed red CP light emission with a $|g_{\text{lum}}|$ of 9×10^{-4} through a mechanism of intramolecular chiral exciton coupling.[24] *N*-Alkylation with chiral alkyl chains has been very recently explored as a synthetic tool for endowing DPP with chiroptical properties either as supramolecular aggregates, whose formation was triggered by hydrogen bonding,[7] or as thin films which were mapped by Mueller Matrix Polarimetry.[16] Moreover, *N*-dihydrocitronellyl chains have been used in a series of DPP-thiophenes to trigger ECD activity in the solution aggregates. The thiophene rings were functionalized with phenyl, 4-(diphenylamino)phenyl or tetraphenylethylene (TPE) substituents; the former two gave intense ECD spectra of the aggregates in solution, whereas TPE yielded no measurable optical activity.[17] Due to the distance between the stereogenic carbon and the DPP core, isolated molecules remained CD silent in solution in all the derivatives.[17]

In general, all the studies on chiral DPP dyes refer to emissive properties in solution, as for those derivatives, ACQ appeared to be dominant in the solid phases. In some cases, the ACQ phenomenon can be prevented by using molecular motifs displaying the property of aggregation-induced emission (AIE) that is the opposite phenomenon to ACQ. AIE is generally explained as an increased rate of radiative relaxation upon molecular aggregation, due to the blocking of intramolecular motion that would otherwise result in fluorescence quenching. Tetraarylethylenes, siloles, and cyanostilbenes are some of the most well-known motifs displaying AIE properties and they, especially TPE, are also some of the most accessible forms from a synthetic point of view.[33] Thanks to the practical access to 1,2,2-(triphenyl)ethylene boronic derivative, it is possible to generate various tetraarylethylene functions on other chromophoric scaffolds by Suzuki coupling, provided the presence of reactive aryl halide sites on the substrate. Following this strategy, TPE-DPP derivatives have been synthesized and studied by Tang and coworkers (Fig. 1).[34] However, although containing TPE moieties, most of the *N*-octyl alkylated DPPs

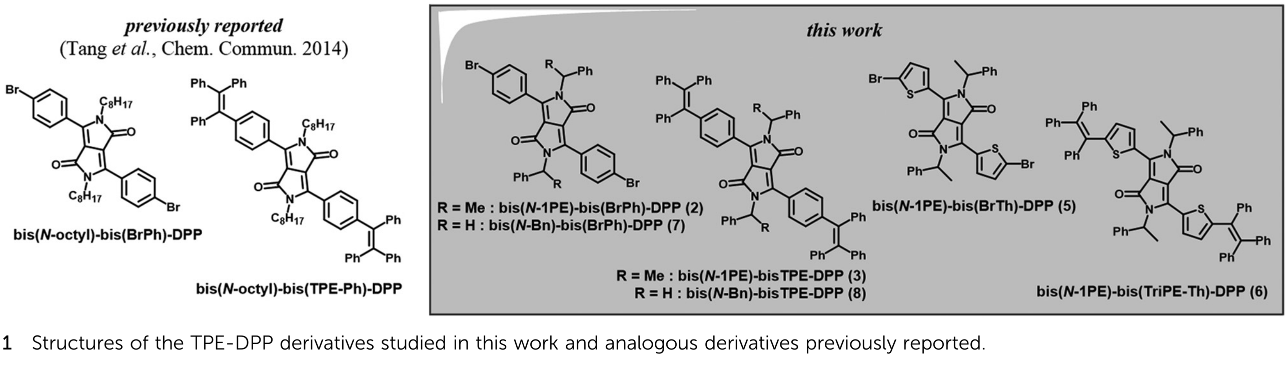

Fig. 1 Structures of the TPE-DPP derivatives studied in this work and analogous derivatives previously reported.

reported in this work displayed ACQ behaviour. A partial AIE phenomenon was only observed upon further modification of the molecules by adding phenyl spacers between DPP cores and TPE functions, and by the introduction of electron-donating amino groups on the TPE portion of the molecule, which seemed to promote ordered aggregation.[34]

Besides the enhanced emissive properties of TPE derivatives in the aggregated state, the use of this structural motif in molecular materials with chiroptical properties is also motivated by the fact that TPE does not remain flat but rather adopts a propeller-shaped conformation, and therefore, upon restriction of molecular motion, the structure can be blocked in one of the two possible enantiomeric conformations characterized by enhanced chiroptical responses.[35–37]

In this work, we aimed at obtaining chiral DPP-based materials with enhanced emissive and chiroptical properties in the solid state. To achieve such a goal, we took advantage of TPE functions applied to a new class of chiral DPP derivatives possessing stereogenic carbons directly connected at the *N*-position (Fig. 1).

2. Results and discussion

2.1 Synthesis and crystal structures of DPP-TPE derivatives

Starting from bis(*p*-bromophenyl)DPP (**1**) that was synthesized according to a previously reported procedure,[34] the two enantiomers of the corresponding bis-(*N*-*sec*-phenethyl)-DPP (**2*RR*** and **2*SS***) were obtained through the newly reported enantioselective protocol based on the Mitsunobu reaction with enantiopure 1-phenylethanol reagents.[38] The chiral TPE-DPP derivatives (**3**) were finally obtained by Suzuki–Miyaura coupling between **2** and pinacol 1,2,2-triphenylethenylboronate (**TPE-Bpin**).[34] A thienyl analogue of TPE-DPP was also synthesized starting from the commercially available bis(2-bromothien-5-yl)DPP (**4**) pigment that was enantioselectively *N*-functionalized with *sec*-phenethyl groups yielding soluble **5*SS*** and **5*RR*** dyes. As for the synthesis of compound **3**, the two enantiomers of chiral bis(5-(1,2,2-triphenylvinyl)thiophen-2-yl)DPP **6*SS*** and **6*RR*** were obtained by Suzuki–Miyaura coupling with **TPE-Bpin** (Scheme 1 and Fig. S1–S6, ESI†).

For comparison purposes, the achiral analogue of **3**, namely the bis(*N*-benzyl)-bisTPE-DPP derivative **8**, has been prepared starting from bis(*p*-bromophenyl)DPP (**1**) upon *N*-benzylation under classical conditions to afford bis(*N*-benzyl)-bis(*p*-bromophenyl)-DPP **7**,[39] followed by the Suzuki–Miyaura coupling of the latter with **TPE-Bpin** (Scheme 2 and Fig. S7, S8, ESI†).

Gratifyingly, single crystals of **3*RR*** and **8** of suitable size for X-ray diffraction were obtained from liquid–liquid diffusion of methanol into *ca.* 10^{-3} M solution in chloroform.

The solid-state structure of **3*RR*** was unambiguously determined by single crystal X-ray diffraction analysis. The compound crystallizes within the non-centrosymmetric space group *P*1,

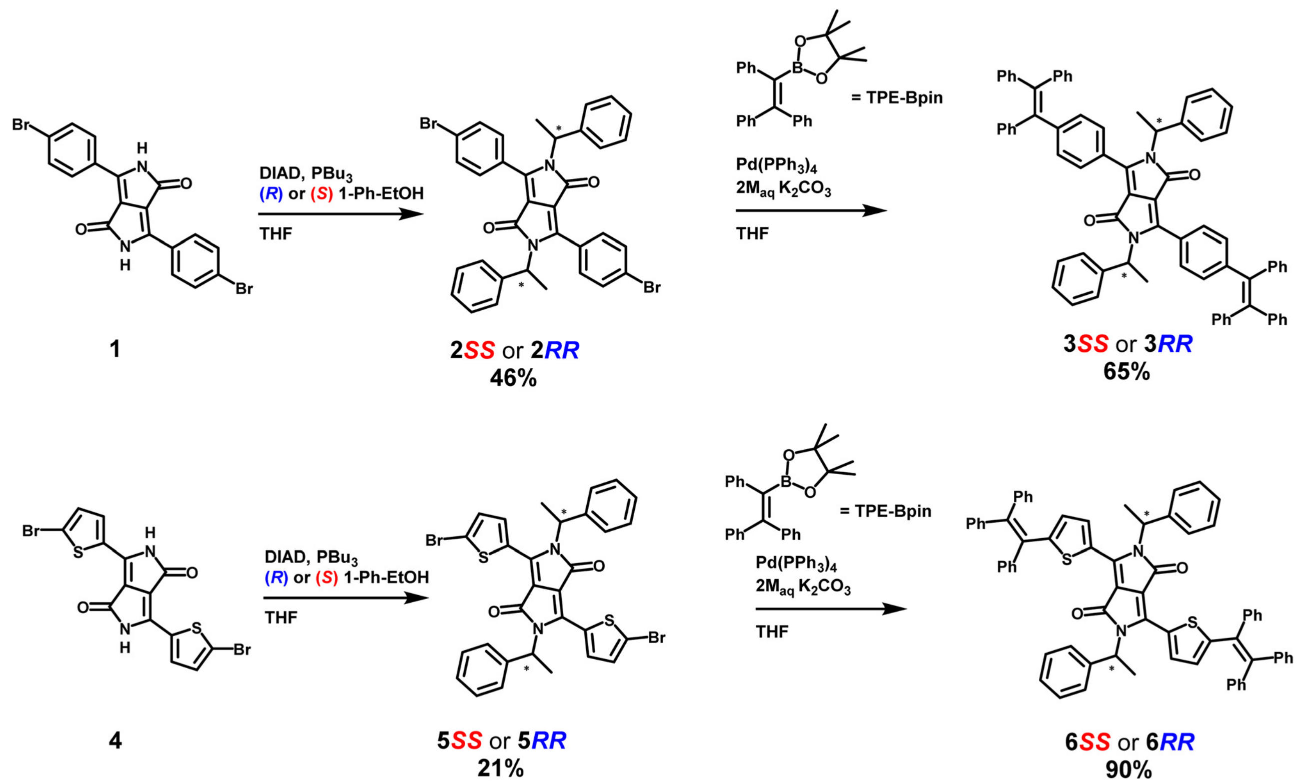

Scheme 1 Synthetic route to chiral TPE-DPP (**3*SS***, **3*RR***, **6*SS*** and **6*RR***) derivatives. During the first step, due to the mechanism of the Mitsunobu reaction, a Walden inversion occurs so that starting from the (*R*)-1-phenylethanol or (*S*)-1-phenylethanol, the ***SS*** and ***RR*** enantiomers are obtained, respectively, for compounds **2** and **5**. The second step consists in a Suzuki–Miyaura coupling between the chiral bromo-derivatives of DPP and **TPE-Bpin**.

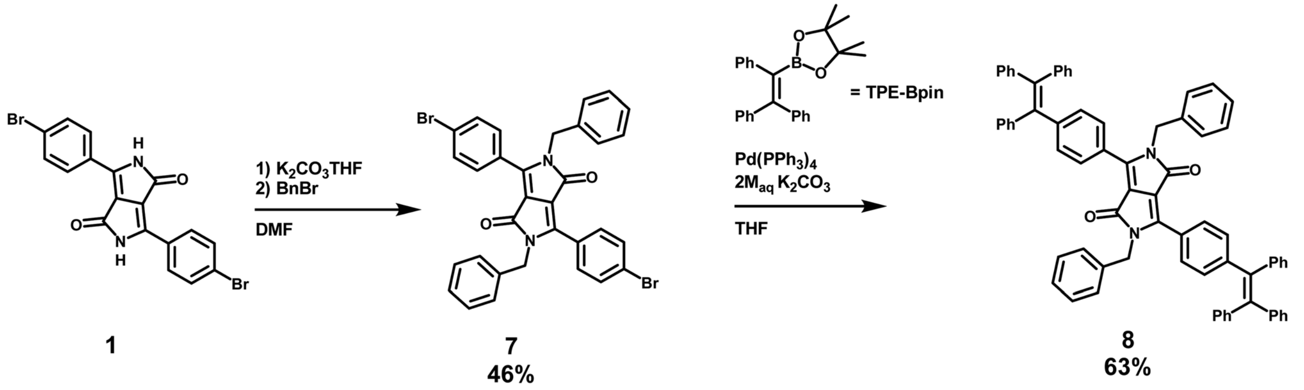

Scheme 2 Synthetic route to the achiral TPE-DPP derivative **8**.

with one independent molecule per asymmetric unit (Tables S1–S3, ESI†). In each molecule, the two TPE moieties adopt complementary conformations which can be defined as *P* and *M* (Fig. 2 and Fig. S9, ESI†).[37] However owing to a network of intramolecular and intermolecular CH–π interactions between asymmetric *sec*-phenethyl groups and TPE moieties, the two TPE moieties are not perfect mirror images to each other.

In the packing, the DPP cores are well isolated by the bulky TPE and *sec*-phenethyl (1-PE) groups (average distance of 9.622 Å between the closest bilactam units), with the occurrence of CH–π intra- and intermolecular interactions (Fig. 3 and Fig. S10, ESI†). Intramolecular TPE-CH to 1-PE π interactions are characterized by distances of 3.066 Å. Intermolecular TPE-CH to 1-PE π interactions have distances of 2.946 Å, while intermolecular 1-PE CH to TPE–π interactions display distances of 2.898 Å.

The torsional angles between the central DPP core and the first phenyl rings ($a{\wedge}\alpha$ and $a'{\wedge}\alpha'$) of the TPE moiety, amounting at *ca.* 40°, have a difference of *ca.* 2° between each side of the molecule, and even smaller differences, of about half degree between the two halves, are measured for the angles between the first phenyl rings of TPE and the plane containing the ethylene system ($\alpha{\wedge}\varepsilon$ and $\alpha'{\wedge}\varepsilon'$) (Fig. 4). Bigger differences are detected for the torsional angles between the ethylene system and the remaining phenyl rings of the TPE moiety ($|\beta{\wedge}\varepsilon - \beta'{\wedge}\varepsilon'| = 3.149°$, $|\gamma{\wedge}\varepsilon - \gamma'{\wedge}\varepsilon'| = 4.390°$, $|\delta{\wedge}\varepsilon - \delta'{\wedge}\varepsilon'| = 3.015°$).

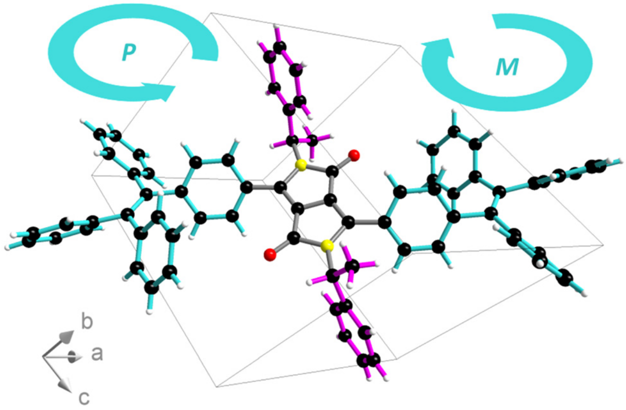

Fig. 2 Structure of **3*RR*** in the crystal phase. The arrows highlight the direction of rotation of the propeller, corresponding to the *P* conformation for the uphill anticlockwise direction, and *M* for the clockwise. The TPE moieties are highlighted in blue and the *sec*-phenethyl groups are highlighted in pink.

On the other hand, compound **8** crystallizes within the centrosymmetric space group $P\bar{1}$, with the half molecule within the asymmetric unit. Therefore, the two TPE units adopt perfect complementary *M* and *P* conformation within each molecule. Similar to **3*RR***, the TPE moieties help keep the DPP isolated, as suggested by the average distance of 9.575 Å between the closest bilactam units (Fig. S11, S12, Tables S1 and S4, S5, ESI†).

2.2 Photophysical study

The enantiomers of compound **2** in 5×10^{-5} M solutions in chloroform display an unresolved absorption band peaking at 469 nm (ε = 28 000 L mol^{-1} cm^{-1}), classically attributed to the π–π* transitions in phenyl-flanked DPP derivatives. Replacing the solvent by a chloroform/methanol (1 : 9) mixture determines a blue shift of 8 nm, without affecting the shape of the peak (Fig. 5a). The ECD spectra show a signal of *ca.* +7.6 L mol^{-1} cm^{-1} for the (*S*,*S*) enantiomer (**2*SS***) at the maximum of the main transition, with a perfect mirror image for the (*R*,*R*) enantiomer (**2*RR***), whose amplitude does not evolve upon a change in the solvent (Fig. 6a). Similarly, the enantiomers of compound **3** show an unresolved absorption band peaking at 486 nm (ε = 24 500 L mol^{-1} cm^{-1}) in chloroform and 475 nm (ε = 18 900 L mol^{-1} cm^{-1}) in the chloroform/methanol (1 : 9) mixture (Fig. 5a). This transition is ECD active as well with a signal amplitude of +4.6 L mol^{-1} cm^{-1} for the (*S*,*S*) enantiomer (**3*SS***), and with a mirror image pattern for the (*R*,*R*) enantiomer (**3*RR***). The absolute value of the intensity of the main ECD band slightly decreases to +3.5 L mol^{-1} cm^{-1} in the chloroform/methanol (1 : 9) mixture (Fig. 6b).

Compound **5** in 10^{-5} M solutions in chloroform displays an absorption band peaking at 525 nm (ε = 15 700 L mol^{-1} cm^{-1}) that appears slightly structured as in other thienyl-DPP derivatives, but not resolved. Replacing the solvent by a chloroform/methanol

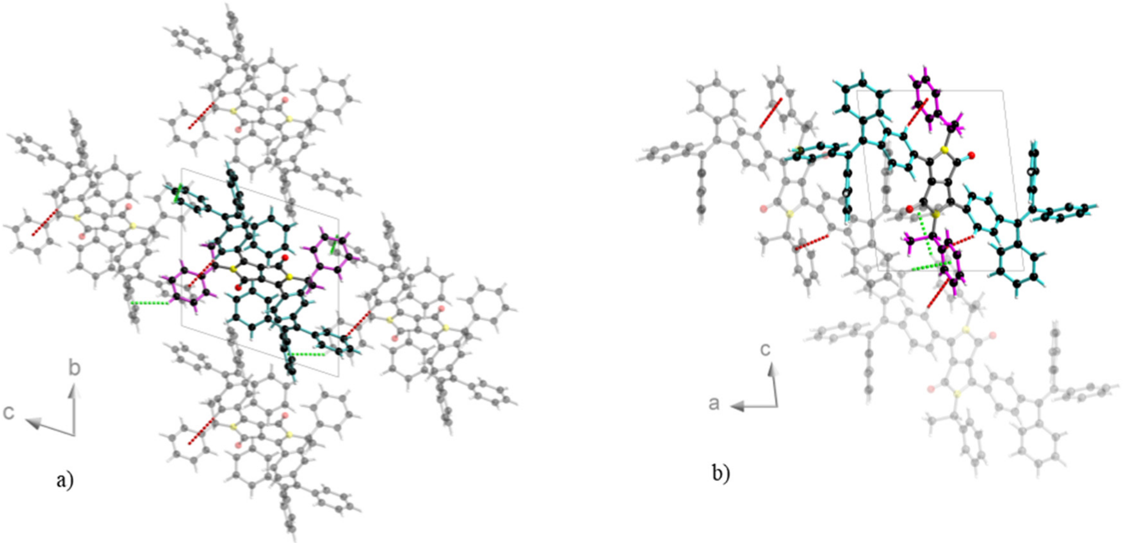

Fig. 3 Crystal packing of **3*RR***, with views along the *a* direction (a), and the *b* direction (b). TPE moieties are highlighted in blue and *sec*-phenethyl (1-PE) groups are highlighted in pink. Intramolecular (red dotted lines) and intermolecular (green dotted lines) CH–π interactions between TPE and 1-PE groups are shown.

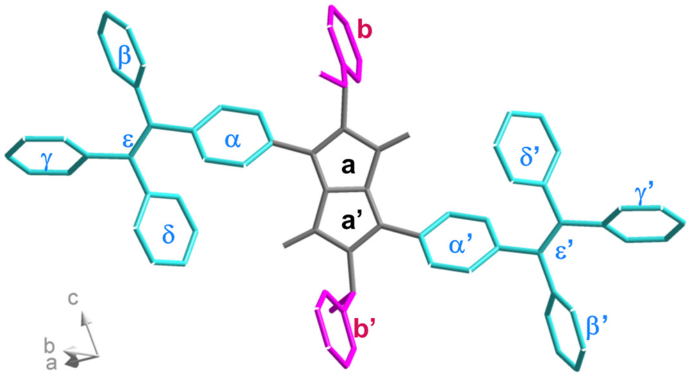

upper half		lower half		
angle	|measure| (deg)	angle	|measure| (deg)	|difference|
a^α	38.751	a'^α	40.970	2.219
α^ε	53.224	α'^ε'	53.808	0.584
β^ε	51.186	β'^ε'	54.335	3.149
γ^ε	46.316	γ'^ε'	50.706	4.390
δ^ε	55.780	δ'^ε'	52.765	3.015
a^b	47.788	a'^b'	46.155	1.633

Fig. 4 Torsional angles between rings within the structure of **3*RR*** in the crystal phase.

(1 : 9) mixture determines a blue shift of 6 nm and a slight hypochromism with a decrease of ε to 14 000 L mol^{-1} cm^{-1} (Fig. 5a). The ECD spectroscopy shows a signal of *ca.* +3.7 L mol^{-1} cm^{-1} for the (*S*,*S*) enantiomer (**5*SS***) at the maximum of the main transition, with a perfect mirror image for the (*R*,*R*) enantiomer (**5*RR***) that does not evolve in the chloroform/methanol (1 : 9) mixture (Fig. 6c). Similarly, the enantiomers of compound **6** show an absorption band peaking at 548 nm (ε = 29 500 L mol^{-1} cm^{-1}) in chloroform and 538 nm in the chloroform/methanol (1 : 9) mixture with a slight hypochromism (ε = 28 700 L mol^{-1} cm^{-1}) (Fig. 5a). This transition is ECD active as well, with a signal amplitude of +7.6 L mol^{-1} cm^{-1} for the (*S*,*S*) enantiomer (**6*SS***) and a mirror image pattern for the (*R*,*R*) enantiomer (**6*RR***). The absolute value of the ECD intensity decreases to +6.4 L mol^{-1} cm^{-1} in the chloroform/methanol (1 : 9) mixture (Fig. 6d).

In the film, the absorption spectra of compounds **2** and **3** broaden and the main peaks are 18 nm and 9 nm red-shifted, respectively. Films of **5** and **6** display a broadened absorption, with 37 nm and 16 nm red shift, respectively, compared to chloroform solutions. The compound **5** exhibits a remarkable red-shift in the solid phase compared to solution. This can be explained as an increased contribution of the low energy shoulder (Fig. 5b), which can be attributed to an increased contribution from J aggregates.[40]

Compound **2** in 3 × 10^{-5} M chloroform solutions, under excitation at 468 nm, shows emission peaking at 548 nm, with a shoulder at 562 nm, with a quantum yield of 82% (Fig. 7a). Compound **3** in 4 × 10^{-5} M chloroform solutions emits light at 564 nm, with a shoulder at 606 nm, with a quantum yield of 25% (Fig. 7a). Compound **5** in 6 × 10^{-5} M chloroform solution emits light with a vibronic progression peaking at 582 nm, 628 nm and 692 nm, with a quantum yield of 63% (Fig. 7a). Compound **6** in 3 × 10^{-5} M chloroform solution emits light at 622 nm, with a shoulder at 672 nm, with a quantum yield of 55% (Fig. 7a).

In solid samples: compound **2** emits within an unresolved band peaking at 547 nm with a quantum yield of 13%.

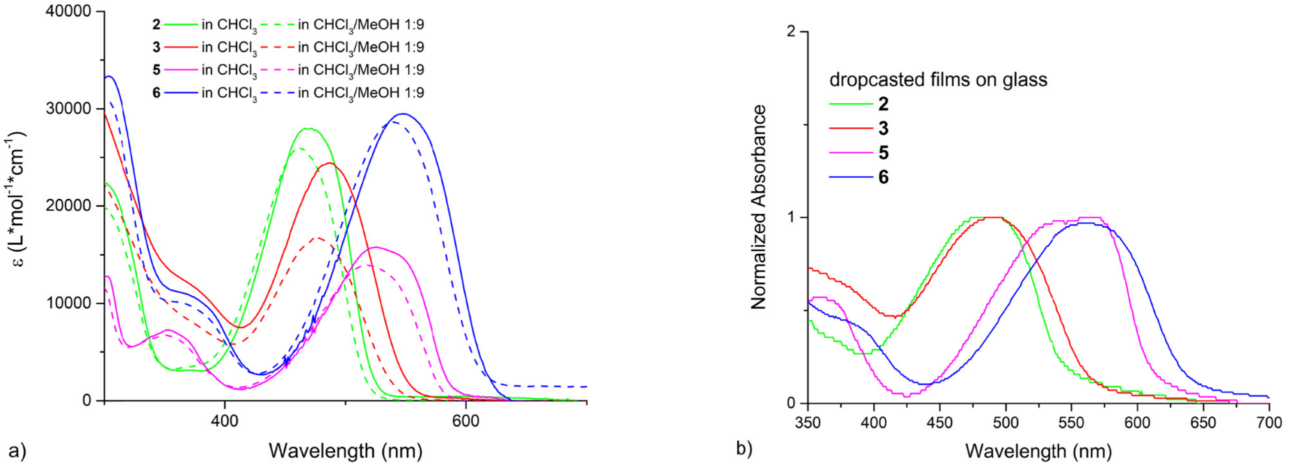

Fig. 5 Molar extinction coefficient spectra in solution (a), and normalized absorption spectra in the film (b). Absorption spectra in solution are measured at a concentration of 5×10^{-5} M in chloroform (continuous line) or in a mixture of chloroform (10% by volume) and methanol. Films are deposited by drop casting from 10^{-4} M solutions in chloroform on glass slides.

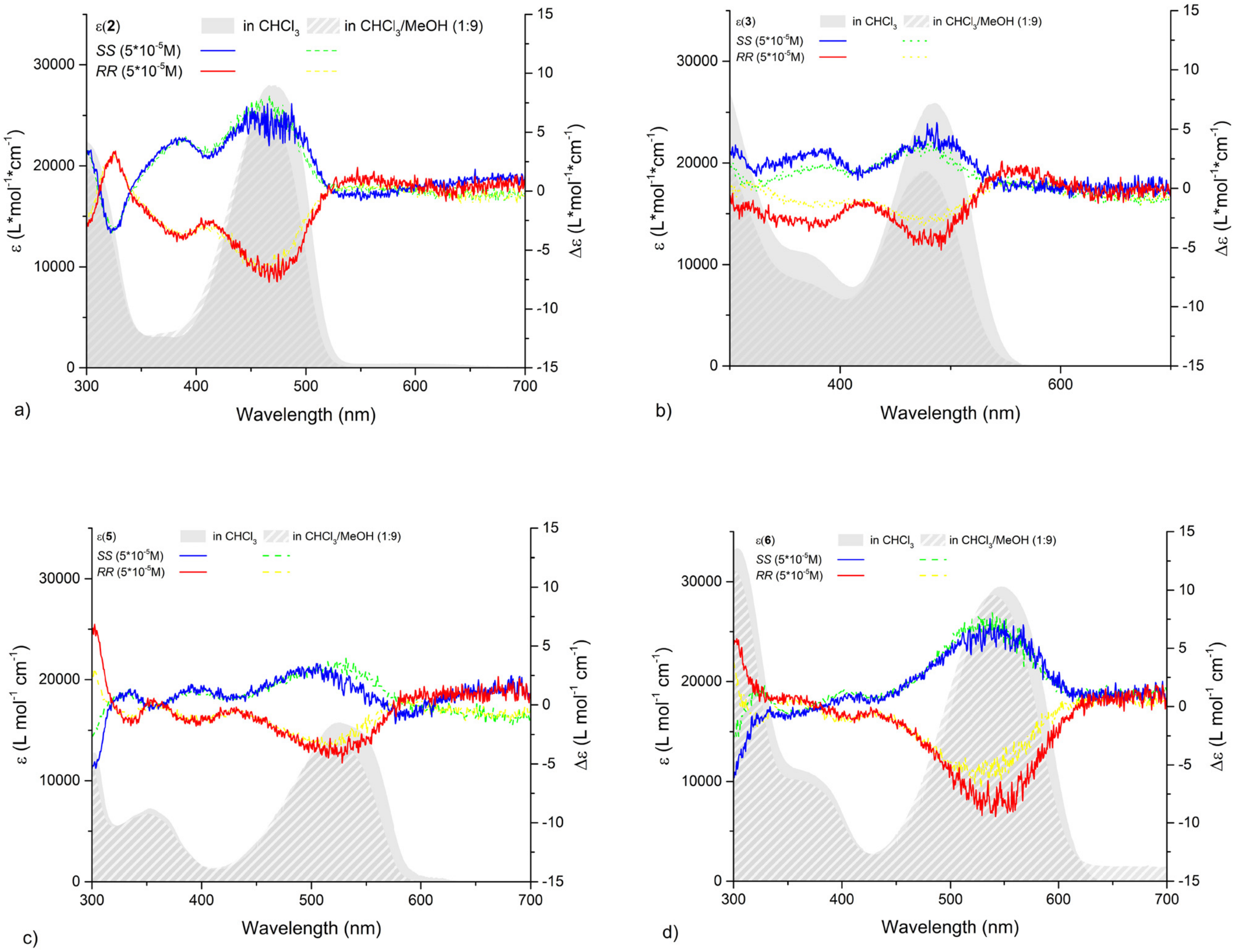

Fig. 6 ECD spectra for each couple of enantiomers (**SS** in blue and green, **RR** in red and yellow) in 10^{-5} M solutions in chloroform (continuous blue and red lines) or chloroform 10% (v/v) in methanol (dashed green and yellow lines), for compounds **2** (a), **3** (b), **5** (c), and **6** (d). In grey shade are shown the corresponding molar extinction coefficient spectra.

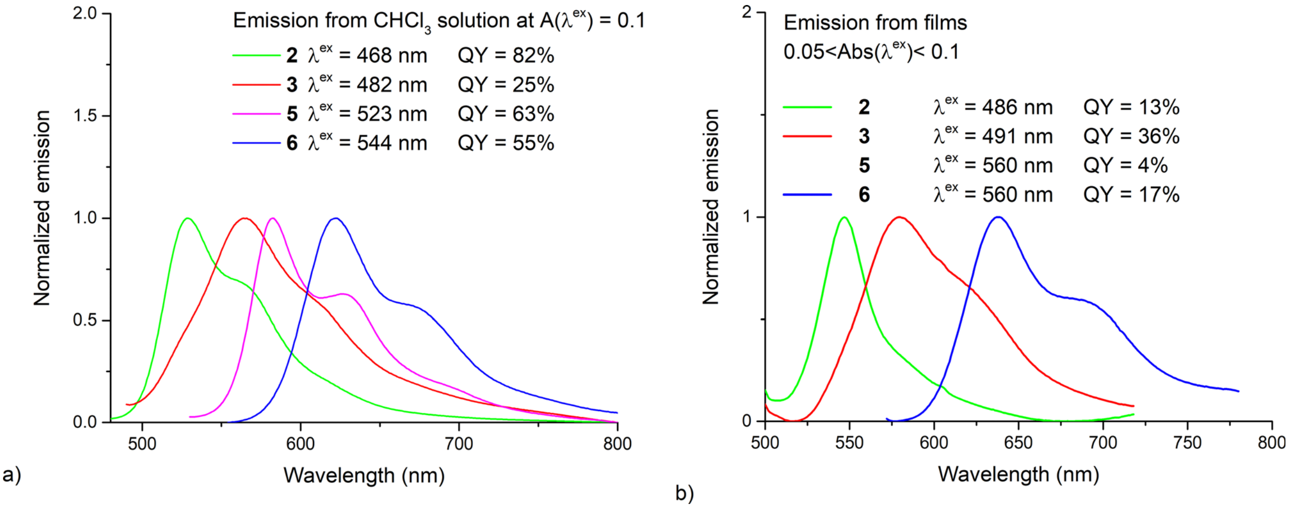

Fig. 7 Photoluminescence spectra from chloroform solutions (a) and films (b). Solutions have a concentration that corresponds to an absorbance of 0.1 in a 10 mm cell, at the excitation wavelength noted in the legend. Similarly, films have an absorbance between 0.05 and 0.1. Fluorescence spectra from compound **5** are not shown. Quantum yields are measured using an integrating sphere, in $CHCl_3$ solutions and on powders at absorptances between 0.05 and 0.15.

Compound **3** shows an emission band peaking at 579 nm, with a shoulder at *ca.* 621 nm and a quantum yield of 36%. Compound **5** emits very weak photoluminescence, whose profile is not shown in Fig. 7b as it is dominated by noise, corresponding to a quantum yield not exceeding 4%. Compound **6** emits an almost resolved vibronic progression starting at 637 nm, with a second peak at 689 nm, and a quantum yield of 17%. Finally, compound **8** emits fluorescence at 594 nm, with a shoulder at 621 nm, and a quantum yield of 27%.

In summary, compounds **2** and **5** are affected by ACQ as expected, even if residual fluorescence is still detectable from compound **2** in the solid state. Conversely, compounds **3** and **6** are not completely quenched in solution, thus they cannot be considered as AIE-gens. However, compound **3** displays an enhanced fluorescence in the solid compared to the solution, therefore it is possible to claim an aggregation-enhanced emission (AEE) for this compound. Indeed, the difference between AIE and AEE phenomena lies in the fact that in the former case, the fluorophore is (almost) totally quenched in solution, while in the latter case, the fluorescence quenching is only partial. On the other hand, compound **6** displays a classic ACQ behaviour despite the presence of a tetraarylethylene system. This can be ascribed to the lower steric demand of thiophene rings, compared to phenyls, which can accommodate into a more planar structure prone to π-stacking interactions.

All the compounds display detectable ECD signals all over the UV-vis absorption region, indicating that introduction of chiral *N*-substituents provides significant perturbation to the extended chromophores. However, in any case, the signals do not seem to evolve upon aggregation. Under the hypothesis that in the solid state, compounds adopt fewer and more precise preferential conformations, thus enhancing ECD features, measurements on dropcast films, and the powders were dispersed into KBr pellets. Unfortunately, all the measurements were not conclusive as these were heavily affected by artefacts.

2.3 Theoretical study

To further investigate the electronic and optical properties of the TPE-DPP derivatives, the electronic structures of the most stable conformations of compounds **2*RR*** (Fig. S13–S20, ESI†), **2*SS*** (Fig. S21–S28, ESI†), **3*RR*** (Fig. S29–S32, ESI†), **3*SS*** (Fig. S33–S36, ESI†) and **8** (Fig. S37–S41, ESI†), in the gas phase, were calculated using a Density Functional Theory (DFT) approach for the ground state and a Time Dependent DFT method for the optical properties. Both the hybrid functional PBE0[41] and the TZVP[42] basis set have been used with the Gaussian 09 program.[43] The ground states have been verified as minima on the potential energy surface with a frequency calculation. The molecular orbital and electron density differences in isosurfaces were calculated and represented with a homemade python program[44] based on cclib.[45] The energy gaps between the HOMO and LUMO of compounds **2**, **3**, and **8** are 3.1 eV, 2.95 eV, and 2.82 eV, respectively, and correspond to transitions with π–π* character mostly located on the DPP core.

The simulated absorption spectrum of the achiral compound **8** shows four relevant absorption bands, the first at 521 nm (π–π* mainly located on the DPP core), the second at 410 nm (π–π* mainly located on the DPP core with the ethylene moieties of TPE), the third at 346 nm (π–π* extended on the whole conjugated system), and the fourth at 320 nm (π–π* mainly located on the TPE moieties), as shown in Fig. S40 (ESI†). Compared to the experimental spectrum (Fig. S42 (ESI†), black line), the lowest energy simulated transition appears overestimated by around 23 nm, while the transitions at 410 nm and 346 nm can be associated to the large bump around 374 nm in the experimental spectrum.

The simulated spectrum of compound **2** shows two relevant absorption bands, the first at 462 nm (π–π*) and the second at 310 nm (n–π*), shown in Fig. S19a and S27a (ESI†), in good agreement with the experiment. The rotational strengths that are calculated as +1.9 × 10^{-40} esu^2 cm^2 at 462 nm and −80.7 × 10^{-40} esu^2 cm^2 at 310 nm for the ***RR*** enantiomer are not accurately reproduced in the ECD spectra, suggesting the presence of many conformations contributing to the experimental spectra.

On the other hand, the simulated spectra of ***RR*** and ***SS*** enantiomers of compound **3** show four relevant absorption bands, the first at 502 nm (π–π*, Fig. 8a), the second at 402 nm (π–π* with larger involvement of the TPE moieties, Fig. 8b), the third including two lines at 345 nm and 343 nm (with n–π* character partially involving the oxygen non-bonding electron pairs and the *N-sec*-phenethyl group, Fig. 8c and d), and the fourth at 321 nm (mainly located on the TPE moiety, Fig. 8e). Compared to the experimental spectrum, the lowest energy transition appears overestimated by around 16 nm, while the cluster of transitions between 402 nm and 343 nm can be associated to a large bump at around 374 nm in the experimental spectrum. The rotational strengths are calculated as −16.4 × 10^{-40} esu^2 cm^2 at 502 nm, −11.7 × 10^{-40} esu^2 cm^2 at 402 nm, −4.5 × 10^{-40} esu^2 cm^2 at 345 nm, −8.4 × 10^{-40} esu^2 cm^2 at 343 nm and 6.5 × 10^{-40} esu^2 cm^2 at 321 nm for the ***RR*** enantiomer that are consistent with the fact that the sign of experimental ECD bands remains negative over a wide wavelength range.

2.4 AEE and CPL study

The photoluminescence behaviour of compounds **3** and **8** was further studied in aggregate states in a series of THF/water mixtures (Fig. 9). Compound **3** shows a 2-fold enhancement of the fluorescence intensity when the water fraction increases from 0% to 70%, accompanied by an increase in the quantum yield from 17% up to 28%. At higher water fraction values, up to 90% of water, intensity and quantum yield decrease slightly. On the other hand, compound **8** shows a 3.5-fold enhancement of the fluorescence intensity when the water fraction increases from 0% to 50%, accompanied by an increase in the quantum yield from 20% up to 58%. Once again, a further increase in water content makes fluorescence intensity and quantum yield gradually drop (Fig. 9). This behaviour has also been reported in a recent work on chiral fluorophores displaying AEE properties, and attributed to the formation of a precipitate.[46]

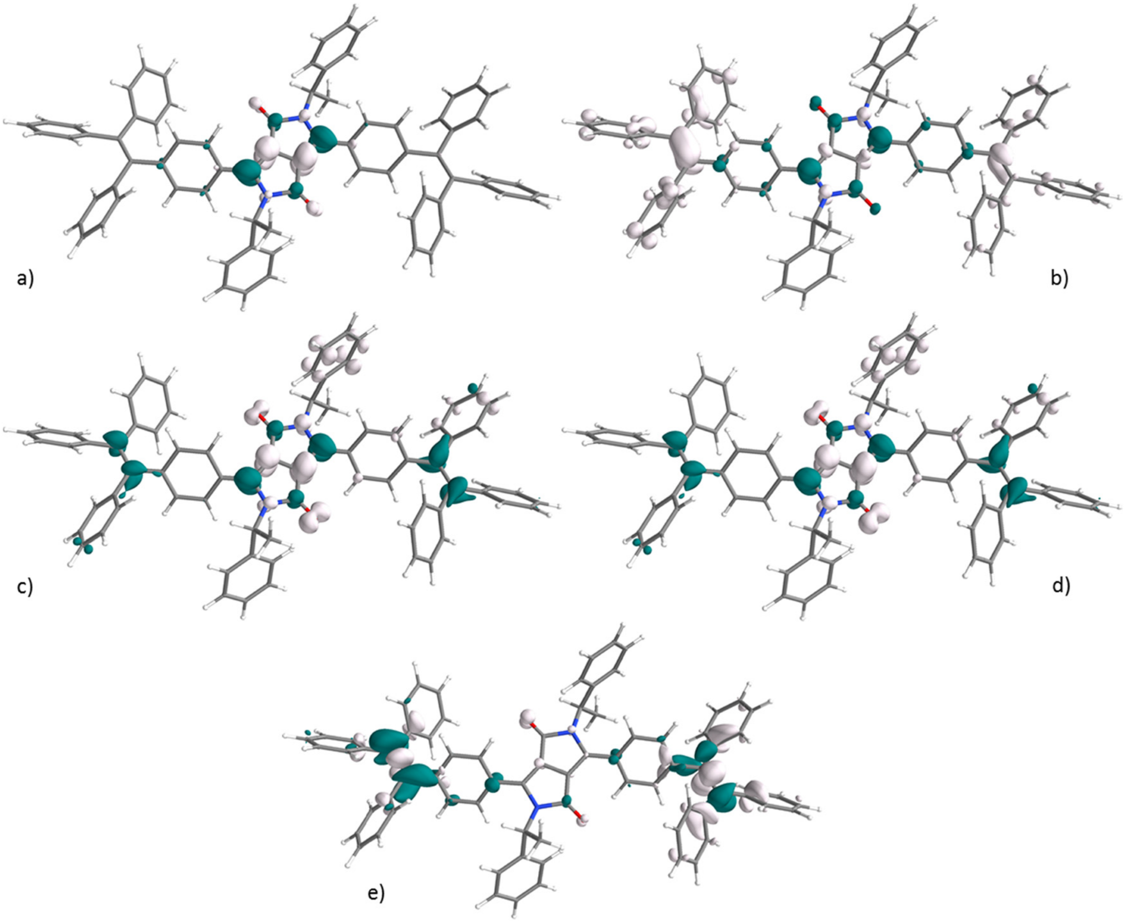

Fig. 8 Representation of the Electron Density Difference (EDD) associated to the strongest transitions calculated for the compound ***3RR***: (a) S0–S1; (b) S0–S3; (c) S0–S6; (d) S0–S7; (e) S0–S8; excited electrons and holes indicated by the green and white surfaces, respectively.

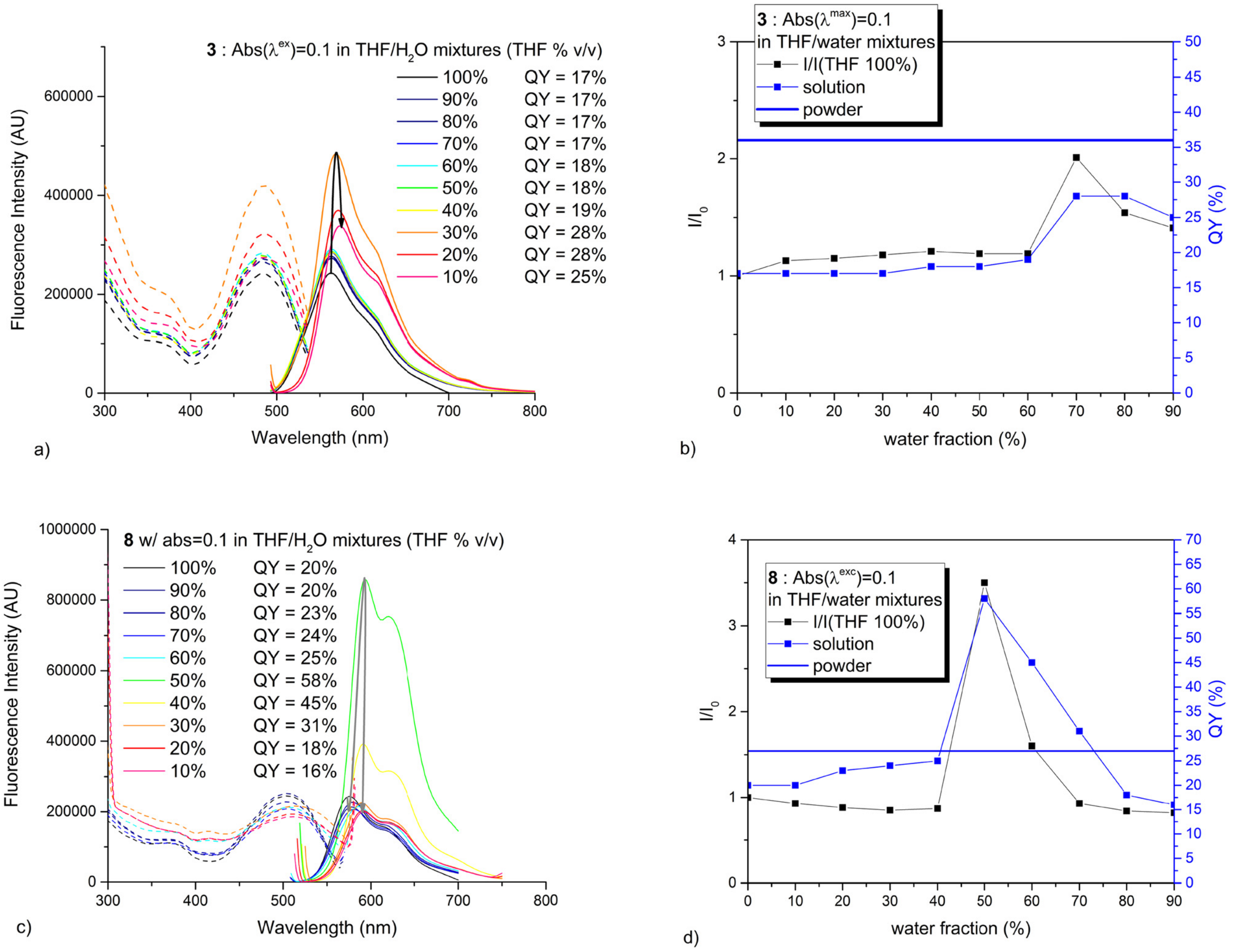

Fig. 9 Emission and excitation spectra of compounds **3** and **8** in THF/water mixtures, displaying the corresponding values of fluorescence quantum yield and I/I_0 ratio. In details: (a) emission (solid lines) and excitation (dashed lines) spectra of **3** in a series of THF/water mixtures, from 100% THF (black lines) to 10% THF (red lines), with respective quantum yield (QY) values; (b) diagram of quantum yield and I/I_0 ratio for **3**, as a function of the water fraction, I_0 being the intensity of the emission peak in pure THF; (c) emission (solid lines) and excitation (dashed lines) spectra of **8** in a series of THF/water mixtures, from 100% THF (black lines) to 10% THF (red lines), with respective quantum yield (QY) values; (d) diagram of quantum yield and I/I_0 ratio for **8**, as a function of the water fraction, I_0 being the intensity of the emission peak in pure THF.

Compound **3** dissolved at a concentration of 10^{-6} M in $CHCl_3$ emitted detectable CPL under excitation at 365 nm, with $|g_{lum}|$ around 2×10^{-4}, with positive values for the ***SS*** enantiomer, and negative for ***RR*** (Fig. S43, ESI†). The sign and magnitude of g_{lum} are coherent with the absorption dissymmetry factor associated to the most red shifted Cotton effect in the ECD spectrum. The B_{CPL} value was estimated to be approximately 0.6 M^{-1} cm^{-1}.[21]

3. Conclusion

In summary, four pairs of enantiomers of organic fluorescent tetraarylethylene-DPP derivatives (***RR*** and ***SS*** enantiomers of compounds **2**, **3**, **5**, and **6**), bearing α-chiral *N*-substituents have been synthesized and characterised. Single-crystal X-ray diffraction experiments revealed that compound **3** adopts complementary *M* and *P* conformations for the two TPE moieties, although not as perfect mirror images. The DFT calculation confirmed that despite the complementary *M* and *P* conformation, a non-negligible rotational strength is associated with all the electronic transitions. All of them displayed ECD activity extended to all the UV-vis absorption features. Further studies on fluorescence emission of compound **3** and its achiral homologue **8** in the THF/water mixture showed that both have AEE properties, exhibiting higher fluorescence quantum yields in aggregate states formed as the water fraction increases. These results are consistent with the fact that they are remarkably fluorescent in the solid state.

To this point, it is important to highlight the role of benzyl-type *N*-substituents, thanks to their steric demand in preventing π–π stacking interactions and ACQ. Indeed, while previously reported analogous TPE-DPP derivatives *N*-alkylated with linear alkyl chains displayed fluorescence quantum yields of 11% in the solid state, compound **8** and **3** (*N*-alkylated with increasing sterically demanding benzyl and *sec*-phenethyl groups, respectively) reached quantum yield values of 27% and 36%, respectively.

These results suggest an interesting direction towards the development of DPP-based fluorophores with enhanced emission in the aggregated states, capable of emitting circularly polarized light with the possibility of increasing g_{lum} factors upon control of the aggregation mode. The combination of chiroptical activity with the aggregation-induced phenomena is indeed expected to attract great interest in the development of new fluorescent probes for imaging[47–49] that would thus be amenable to be stimulated and/or read under circularly polarised light with the potential enhancement of the signal-to-noise ratio.

4. Experimental section

4.1 Materials and methods

All commercially available reagents and solvents were used as received unless otherwise noted. Dry tetrahydrofuran was directly used from the purification machines. Chloroform as a solvent for synthesis was distilled over calcium hydride prior to use. Chromatography purifications were performed on the silica gel Sorbent Technologies Silica Gel (60 Å, 65 × 250 mesh) and thin layer chromatography (TLC) was carried out using aluminum sheets precoated with silica gel 60 (EMD 40–60 mm, 230–400 mesh with 254 nm dye). All reactions were carried out in Schlenk tubes under an argon atmosphere. Dropwise additions were performed using a programmable syringe pump. NMR spectra were acquired on Bruker Avance DRX 300 and 500 spectrometers operating at 300 and 500 MHz for ^{1}H and 75 and 125 MHz for ^{13}C, respectively, at room temperature in $CDCl_3$ solutions. ^{1}H and ^{13}C NMR spectra were referenced to the residual protonated solvent (^{1}H) or the solvent itself (^{13}C). All chemical shifts are expressed in parts per million (ppm) downfield from external tetramethylsilane (TMS), using the solvent residual signal as an internal standard and the coupling constant values (*J*) are reported in Hertz (Hz). The following abbreviations have been used: s, singlet; dd, doublet of doublets; m, multiplet. Mass spectrometry MALDI–TOF MS spectra were recorded on a Bruker Biflex-IIITM apparatus, equipped with a 337 nm N_2 laser.

The spectroscopic properties of the derivatives **2**, **3**, **5** and **6** were evaluated in solutions at concentrations of 5×10^{-5} M for absorption measurements on a Shimadzu UV-1800 spectrometer, and at adjusted concentrations corresponding to an absorbance of 0.1 for fluorescence measurements on an RF-6000 fluorimeter. The absorption spectroscopy and circular dichroism spectroscopy of **2**, **3**, **5** and **6** as isolated molecules were recorded in chloroform solutions on a JASCO J-1500 spectrometer at 20 °C, while in order to assess the effect of aggregation, a mixture of chloroform/methanol (1 : 9) was used as a solvent, by keeping the solute concentration at 5×10^{-5} M.

Spectrophotometry and fluorimetry in the solid state were recorded on films of **2**, **3**, **5** and **6** drop-casted from 10^{-4} solutions in $CHCl_3$ onto glass slides. Fluorescence quantum yields were measured on a JASCO FP-8500 fluorimeter equipped with an integrating sphere, in 5×10^{-5} chloroform solutions and in solid powder spread between glass slides, with absorptance between 0.05 and 0.15 (average on 4 measures). CPL spectra of **3*RR*/3*SS*** were recorded in 10^{-6} M $CHCl_3$ solution with a home-built instrument under 365 nm irradiation by using a 90° geometry between excitation and detection.[50]

4.2 Synthesis

Synthesis of 2,5-bis((*S*)-1-phenylethyl)-3,6-bis(4-(1,2,2-triphenylvinyl)phenyl)-2,5-dihydropyrrolo [3,4-*c*]pyrrole-1,4-dione (3*SS*). In a Schlenk tube, **2*SS***[38] (50 mg, 0.076 mmol, 1 eq.), **TPE-Bpin**[34] (64 mg, 0.168 mmol, 2.2 eq.), and $Pd(PPh_3)_4$ (2.7 mg, 0.0023 mmol, 0.03 eq.) were charged and purged with three vacuum/argon cycles. THF (2.5 mL) and aqueous K_2CO_3 (2 M, 0.8 mL, 20 eq.), previously degassed, were injected into the reaction vessel, and the resulting mixture was stirred at reflux overnight. Once the reaction completed, the crude was extracted into dichloromethane and washed with water. The organic layer was dried over anhydrous $MgSO_4$ and the solvent was removed under reduced pressure. The crude was purified by silica gel column chromatography with a mixture of petroleum ether/dichloromethane (3 : 2) as the eluent, affording 49 mg (64% yield) of **3*SS*** as a bright orange powder.

Similarly, **3*RR*** was obtained from **2*RR*** following the same procedure.

^{1}H NMR (300 MHz, $CDCl_3$) δ = 7.33–7.19 (m, 16H), 7.15–6.99 (m, 32H), 5.29 (q, *J* = 6.9 Hz, 2H), 1.77 (d, *J* = 7.1 Hz, 6H) ppm.

^{13}C NMR (76 MHz, $CDCl_3$) δ = 163.01, 149.06, 146.80, 143.58, 143.39, 142.96, 142.59, 141.60, 141.53, 140.35, 131.71, 131.52, 131.39, 128.57, 127.99, 127.95, 127.81, 127.27, 126.96, 126.85, 126.27, 110.49, 53.22, 18.42 ppm.

HRMS (DCTB, M^+) calcd for $C_{74}H_{56}N_2O_2^+$ 1004.43368; found 1004.43363.

Synthesis of 3,6-bis(5-bromothiophen-2-yl)-2,5-bis((*S*)-1-phenylethyl)-2,5-dihydropyrrolo[3,4-*c*] pyrrole-1,4-dione (5*RR*). Under an argon atmosphere, tributylphosphine (1.08 mL, 4.37 mmol, 5 eq.) was dissolved in dry THF (3 mL) and the mixture cooled at 0 °C, then DIAD (1.03 mL, 4.37 mmol, 5 eq.) was added dropwise, resulting in a rapid loss of DIAD's bright yellow tint upon the formation of a complex with the phosphine. In a separate Schlenk tube, under an argon atmosphere, **4** (400 mg, 0.87 mmol, 1 eq.) was dispersed in dry THF (10 mL) and the mixture cooled at 0 °C. The mixture containing the Bu3P/DIAD complex was added dropwise into the second Schlenk tube resulting in a bluish purple solution. At this point, (*R*)-1-phenylethanol (0.53 mL, 4.37 mmol, 5 eq.) dissolved in THF (1 mL) was injected dropwise to the mixture over 5 h. The mixture was then allowed to reach RT and kept for stirring overnight.

The mixture was poured in 1 M aqueous HCl and extracted into dichloromethane. The organic layer was first washed with water, then dried over anhydrous $MgSO_4$ and the solvent was removed under reduced pressure. The crude was purified by silica gel column chromatography with a mixture of petroleum ether/dichloromethane (2 : 3) as the eluent, affording 120 mg (21% yield) of **5*RR*** as a dark reddish powder.

Similarly, **5*SS*** was obtained from (*S*)-1-phenylethanol following the same procedure.

^{1}H NMR (300 MHz, $CDCl_3$) δ = 7.88 (d, *J* = 4.1 Hz, 2H), 7.38–7.27 (m, 10H), 7.10 (d, *J* = 4.1 Hz, 2H), 5.73 (q, *J* = 7.2 Hz, 2H), 1.96 (d, *J* = 7.1 Hz, 6H) ppm.

^{13}C NMR (76 MHz, $CDCl_3$) δ = 161.74, 140.68, 140.16, 134.44, 131.42, 130.58, 128.81, 127.55, 126.51, 119.29, 109.84, 53.58, 18.39 ppm.

HRMS (DCTB, M^+) calcd for $C_{30}H_{22}N_2O_2S_2Br_2^+$ 663.94910; found 663.94840.

Synthesis of 2,5-bis((*S*)-1-phenylethyl)-3,6-bis(5-(1,2,2-triphenylvinyl)thiophen-2-yl)-2,5-dihydro pyrrolo[3,4-*c*]pyrrole-1,4-dione (*6RR*). **5*RR*** (80 mg, 0.120 mmol, 1eq.), **TPE-Bpin**[34] (101 mg, 0.264 mmol, 2.2 eq.), and $Pd(PPh_3)_4$ (4.2 mg, 0.0036 mmol, 0.03 eq.) were charged in a Schlenk tube and purged with three vacuum/argon cycles. THF (2.5 mL) and aqueous K_2CO_3 (2 M, 1.2 mL, 20 eq.), previously degassed, were injected into the reaction vessel, and the resulting mixture was stirred at reflux overnight. Once the reaction completed, the crude was extracted into dichloromethane and washed with water. The organic layer was dried over anhydrous $MgSO_4$, and the solvent was removed under reduced pressure. The crude was purified by silica gel column chromatography with a mixture of petroleum ether/dichloromethane (2 : 3) as the eluent, affording 100 mg (90% yield) of **6*RR*** as a purple powder.

Similarly, **6*SS*** was obtained from **6*SS*** following the same procedure.

^{1}H NMR (499 MHz, $CDCl_3$) δ = 8.06 (d, *J* = 4.0 Hz, 2H), 7.41–7.31 (m, 8H), 7.30–7.19 (m, 10H), 7.10–7.06 (m, 6H), 7.04 (d, *J* = 4.0 Hz, 2H), 7.03–7.00 (m, 4H), 6.98–6.92 (m, 6H), 6.89–6.85 (m, 4H), 6.68 (s, 2H), 5.61 (q, *J* = 6.8 Hz, 2H), 1.82 (d, *J* = 7.1 Hz, 6H).

^{13}C NMR (125 MHz, $CDCl_3$) δ = 161.90, 149.05, 144.18, 141.79, 140.92, 140.76, 139.65, 137.17, 134.74, 132.61, 131.85, 131.29, 130.80, 130.13, 129.31, 129.00, 128.71, 128.49, 128.45, 128.19, 127.90, 127.86, 127.12, 127.05, 126.57, 109.40, 53.64, 18.11 ppm.

HRMS (DCTB, M^+) calcd for $C_{70}H_{52}N_2O_2S_2^+$ 1016.34529; found 1016.34647.

Synthesis of 2-benzyl-5-(1-phenylethyl)-3,6-bis(4-(1,2,2-triphenylvinyl)phenyl)-2,5-dihydropyrrolo[3,4-*c*]pyrrole-1,4-dione (8). **7** (50 mg, 0.80 mmol, 1 eq.),[39] **TPE-Bpin** (67 mg, 0.175 mmol, 2.2 eq.),[34] and $Pd(PPh_3)_4$ (5.5 mg, 0.0048 mmol, 0.06 eq.) were charged in a Schlenk tube and purged with three vacuum/argon cycles. THF (2.5 mL) and aqueous K_2CO_3 (2 M, 0.8 mL, 20 eq.), previously degassed, were injected into the reaction vessel, and the resulting mixture was stirred at reflux overnight. Once the reaction completed, the crude was extracted into dichloromethane and washed with water. The organic layer was dried over anhydrous $MgSO_4$, and the solvent was removed under reduced pressure. The crude was purified by silica gel column chromatography with a mixture of petroleum ether, dichloromethane and ethyl acetate (20%, 79%, 1% respectively) as the eluent, and then recrystallized from $CHCl_3$/MeOH affording 48 mg (63% yield) of **8** as a bright red powder.

^{1}H NMR (499 MHz, $CDCl_3$) δ = 7.50 (d, *J* = 8.5 Hz, 4H), 7.29–7.22 (m, 4H), 7.14–6.98 (m, 40H), 4.90 (s, 4H) ppm.

^{13}C NMR (125 MHz, $CDCl_3$) δ = 162.92, 148.52, 147.21, 143.44, 143.43, 143.12, 142.69, 140.20, 137.65, 131.86, 131.55, 131.48, 131.41, 128.84, 128.57, 128.03, 127.99, 127.82, 127.47, 127.03, 126.88, 126.86, 125.97, 109.73, 45.79 ppm.

HRMS (DCTB, M^+) calcd for $C_{72}H_{52}N_2O_2^+$ 976.40259; found 976.40233.

4.3 X-Ray structure determination

Details about data collection and solution refinement are given in Table S1 (ESI†). Single crystals of the compounds were mounted on glass fibre loops using a viscous hydrocarbon oil to coat the crystal and then transferred directly to cold nitrogen stream for data collection. Collection of X-ray data was performed at 150 K and ambient temperature on an Agilent Supernova diffractometer with CuKα radiation (λ = 1.54184 Å). The structures were solved by direct methods using the SHELXS-97 and SIR92 programs and refined against all F^2 values with the SHELXL-97 program using the WinGX graphical user interface. All non-H atoms were refined anisotropically. Hydrogen atoms were introduced at calculated positions (riding model), included in structure factor calculations but not refined. Crystallographic data for the two structures have been deposited with the Cambridge Crystallographic Data Centre, deposition numbers CCDC 2237602 (**3*RR***) and CCDC 2153712 (**5**).†

Conflicts of interest

There are no conflicts to declare.

Acknowledgements

The authors thank the CNRS, the University of Angers and the RFI Regional project LUMOMAT (grant to M. M. T., project HinTenSiF). Ingrid Freuze (University of Angers) is gratefully acknowledged for MS characterization and Magali Allain (University of Angers) for help with the X-ray structures. Dr Kévin Martin (Moltech-Anjou) is thanked for help with the CD characterization and Allan Leroy (ETSCO student) is gratefully acknowledged for his contribution in the synthesis of one enantiomer of compounds **5** and **6**.

References

1 F. Song, Z. Xu, Q. Zhang, Z. Zhao, H. Zhang, W. Zhao, Z. Qiu, C. Qi, H. Zhang, H. H. Y. Sung, I. D. Williams, J. W. Y. Lam, Z. Zhao, A. Qin, D. Ma and B. Z. Tang, *Adv. Funct. Mater.*, 2018, **28**, 1800051.

2 K. He, S. Zhou, W. Li, H. Tian, Q. Tang, J. Zhang, D. Yan, Y. Geng and F. Wang, *J. Mater. Chem. C*, 2019, **7**, 3656–3664.

3 Q. Liu, S. E. Bottle and P. Sonar, *Adv. Mater.*, 2020, **32**, 1903882.

4 W. W. Bao, R. Li, Z. C. Dai, J. Tang, X. Shi, J. T. Geng, Z. F. Deng and J. Hua, *Front. Chem.*, 2020, **8**, 1–6.

5 M. Mastropasqua Talamo, F. Pop, P. Hume, M. Abbas, G. Wantz and N. Avarvari, *J. Mater. Chem. C*, 2022, **10**, 8034–8042.

6 B. W. H. Saes, M. Lutz, M. M. Wienk, S. C. J. Meskers and R. A. J. Janssen, *J. Phys. Chem. C*, 2020, **124**, 25229–25238.

7 S. Militzer, N. Nishimura, N. R. Ávila-Rovelo, W. Matsuda, D. Schwaller, P. J. Mésini, S. Seki and A. Ruiz-Carretero, *Chem. – Eur. J.*, 2020, **26**, 9998–10004.

8 X. Shang, I. Song, J. H. Lee, M. Han, J. C. Kim, H. Ohtsu, J. Ahn, S. K. Kwak and J. H. Oh, *J. Mater. Chem. C*, 2019, **7**, 8688–8697.

9 J. Roncali, *Macromol. Rapid Commun.*, 2007, **28**, 1761–1775.

10 J. Gierschner, J. Cornil and H.-J. Egelhaaf, *Adv. Mater.*, 2007, **19**, 173–191.

11 H. Han, Y. J. Lee, J. Kyhm, J. S. Jeong, J.-H. Han, M. K. Yang, K. M. Lee, Y. Choi, T.-H. Yoon, H. Ju, S.-k Ahn and J. A. Lim, *Adv. Funct. Mater.*, 2020, **30**, 2006236.

12 Y. Deng, M. Wang, Y. Zhuang, S. Liu, W. Huang and Q. Zhao, *Light: Sci. Appl.*, 2021, **10**, 76.

13 C. Hao, L. Xu, M. Sun, H. Zhang, H. Kuang and C. Xu, *Chem. – Eur. J.*, 2019, **25**, 12235–12240.

14 J. Han, S. Guo, H. Lu, S. Liu, Q. Zhao and W. Huang, *Adv. Opt. Mater.*, 2018, **6**, 1800538.

15 F. Pop, N. Zigon and N. Avarvari, *Chem. Rev.*, 2019, **119**, 8435–8478.

16 C. E. Killalea, M. Samperi, G. Siligardi and D. B. Amabilino, *Chem. Commun.*, 2022, **58**, 4468–4471.

17 G. Albano, F. Zinna, F. Urraci, M. A. M. Capozzi, G. Pescitelli, A. Punzi, L. Di Bari and G. M. Farinola, *Chem. -- Eur. J.*, 2022, **28**, e202201178.

18 G. Pescitelli, L. Di Bari and N. Berova, *Chem. Soc. Rev.*, 2014, **43**, 5211–5233.

19 Y. Nagata and T. Mori, *Front. Chem.*, 2020, **8**, 1–6.

20 H. Kubo, T. Hirose, T. Nakashima, T. Kawai, J.-y Hasegawa and K. Matsuda, *J. Phys. Chem. Lett.*, 2021, **12**, 686–695.

21 L. Arrico, L. Di Bari and F. Zinna, *Chem. – Eur. J.*, 2021, **27**, 2920–2934.

22 F. Zinna, U. Giovanella and L. D. Bari, *Adv. Mater.*, 2015, **27**, 1791–1795.

23 F. Zinna and L. Di Bari, *Chirality*, 2015, **27**, 1–13.

24 K. Dhbaibi, L. Favereau, M. Srebro-Hooper, M. Jean, N. Vanthuyne, F. Zinna, B. Jamoussi, L. Di Bari, J. Autschbach and J. Crassous, *Chem. Sci.*, 2018, **9**, 735–742.

25 T. Gao, Z. Jiang, B. Chen, Q. Sun, Y. Orooji, L. Huang and Z. Liu, *Dyes Pigm.*, 2020, **173**, 107998.

26 A. Taniguchi, D. Kaji, N. Hara, R. Murata, S. Akiyama, T. Harada, A. Sudo, H. Nishikawa and Y. Imai, *RSC Adv.*, 2019, **9**, 1976–1981.

27 F. Zinna, G. Albano, A. Taddeucci, T. Colli, L. A. Aronica, G. Pescitelli and L. Di Bari, *Adv. Mater.*, 2020, **32**, 2002575.

28 J. Wade, J. N. Hilfiker, J. R. Brandt, L. Liirò-Peluso, L. Wan, X. Shi, F. Salerno, S. T. J. Ryan, S. Schöche, O. Arteaga, T. Jávorfi, G. Siligardi, C. Wang, D. B. Amabilino, P. H. Beton, A. J. Campbell and M. J. Fuchter, *Nat. Commun.*, 2020, **11**, 6137.

29 M. Grzybowski, E. Glodkowska-Mrowka, T. Stoklosa and D. T. Gryko, *Org. Lett.*, 2012, **14**, 2670–2673.

30 M. Grzybowski and D. T. Gryko, *Adv. Opt. Mater.*, 2015, **3**, 280–320.

31 M. A. Naik, N. Venkatramaiah, C. Kanimozhi and S. Patil, *J. Phys. Chem. C*, 2012, **116**, 26128–26137.

32 A. Leventis, J. Royakkers, A. G. Rapidis, N. Goodeal, M. K. Corpinot, J. M. Frost, D.-K. Bučar, M. O. Blunt, F. Cacialli and H. Bronstein, *J. Am. Chem. Soc.*, 2018, **140**, 1622–1626.

33 J. Mei, N. L. C. Leung, R. T. K. Kwok, J. W. Y. Lam and B. Z. Tang, *Chem. Rev.*, 2015, **115**, 11718–11940.

34 X. Y. Shen, Y. J. Wang, H. Zhang, A. Qin, J. Z. Sun and B. Z. Tang, *Chem. Commun.*, 2014, **50**, 8747–8750.

35 J. Roose, B. Z. Tang and K. S. Wong, *Small*, 2016, **12**, 6495–6512.

36 C. Shen, F. Gan, G. Zhang, Y. Ding, J. Wang, R. Wang, J. Crassous and H. Qiu, *Mater. Chem. Front.*, 2020, **4**, 837–844.

37 M. Hu, F.-Y. Ye, C. Du, W. Wang, T.-T. Zhou, M.-L. Gao, M. Liu and Y.-S. Zheng, *ACS Nano*, 2021, **15**, 16673–16682.

38 M. Mastropasqua Talamo, F. Pop and N. Avarvari, *Chem. Commun.*, 2021, **57**, 6514–6517.

39 M. Kamioka, Y. Wang, S. Mori, H. Furuta and S. Shimizu, *Eur. J. Inorg. Chem.*, 2022, e202200081.

40 A. Punzi, D. Blasi, A. Operamolla, R. Comparelli, G. Palazzo and G. M. Farinola, *RSC Adv.*, 2021, **11**, 11536–11540.

41 C. Adamo and V. Barone, *J. Chem. Phys.*, 1999, **110**, 6158–6170.

42 A. Schäfer, C. Huber and R. Ahlrichs, *J. Chem. Phys.*, 1994, **100**, 5829–5835.

43 M. J. Frisch, G. W. Trucks, H. B. Schlegel, G. E. Scuseria, M. A. Robb, J. R. Cheeseman, G. Scalmani, V. Barone, B. Mennucci, G. A. Petersson, H. Nakatsuji, M. Caricato, X. Li, H. P. Hratchian, A. F. Izmaylov, J. Bloino, G. Zheng, J. L. Sonnenberg, M. Hada, M. Ehara, K. Toyota, R. Fukuda, J. Hasegawa, M. Ishida, T. Nakajima, Y. Honda, O. Kitao, H. Nakai, T. Vreven, J. A. Montgomery Jr., J. E. Peralta, F. Ogliaro, M. Bearpark, J. J. Heyd, E. Brothers, K. N. Kudin, V. N. Staroverov, T. Keith, R. Kobayashi, J. Normand, K. Raghavachari, A. Rendell, J. C. Burant, S. S. Iyengar, J. Tomasi, M. Cossi, N. Rega, J. M. Millam, M. Klene, J. E. Knox, J. B. Cross, V. Bakken, C. Adamo, J. Jaramillo, R. Gomperts, R. E. Stratmann, O. Yazyev, A. J. Austin, R. Cammi, C. Pomelli, J. W. Ochterski, R. L. Martin, K. Morokuma, V. G. Zakrzewski, G. A. Voth, P. Salvador, J. J. Dannenberg, S. Dapprich, A. D. Daniels, O. Farkas, J. B. Foresman, J. V. Ortiz, J. Cioslowski and D. J. Fox, *Gaussian 09, Revision D.01*, Wallingford, CT, 2013.

44 T. Cauchy and B. Q. Da Mota, *A python program for control quality and automatic generation of quantum chemistry results*, University of Angers, 2020.

45 N. M. O'Boyle, A. L. Tenderholt and K. M. Langner, *J. Comput. Chem.*, 2008, **29**, 839–845.

46 C. Liu, C. Yuan, G. Shi, K. Jia, J. Liu, K.-P. Wang, S. Chen and Z.-Q. Hu, *Dyes Pigm.*, 2023, **210**, 110992.

47 H. Lu, Y. Zheng, X. Zhao, L. Wang, S. Ma, X. Han, B. Xu, W. Tian and H. Gao, *Angew. Chem., Int. Ed.*, 2016, **55**, 155–159.

48 Y.-L. Wang, C. Li, H.-Q. Qu, C. Fan, P.-J. Zhao, R. Tian and M.-Q. Zhu, *J. Am. Chem. Soc.*, 2020, **142**, 7497–7505.

49 R. Tian, Y.-L. Wang, C. Li and M.-Q. Zhu, *Mater. Chem. Front.*, 2022, **6**, 1188–1193.

50 F. Zinna, T. Bruhn, C. A. Guido, J. Ahrens, M. Bröring, L. Di Bari and G. Pescitelli, *Chem. – Eur. J.*, 2016, **22**, 16089–16098.